Nonreciprocal Dissipation Engineering via Strong Coupling with a Continuum of Modes

Yishu Zhou,[1,*] Freek Ruesink,[1] Shai Gertler,[1] Haotian Cheng,[1] Margaret Pavlovich,[1] Eric Kittlaus,[2] Andrew L. Starbuck,[3] Andrew J. Leenheer,[3] Andrew T. Pomerene,[3] Douglas C. Trotter,[3] Christina Dallo,[3] Katherine M. Musick,[3] Eduardo Garcia,[3] Robert Reyna,[3] Andrew L. Holterhoff,[3] Michael Gehl,[3] Ashok Kodigala,[3] John Bowers,[4] Matt Eichenfield,[3,5] Nils T. Otterstrom,[3] Anthony L. Lentine,[3] and Peter Rakich[1,†]

[1]*Department of Applied Physics, Yale University, New Haven, Connecticut, USA*
[2]*Jet Propulsion Laboratory, California Institute of Technology, Pasadena, California, USA*
[3]*Microsystems Engineering, Science, and Applications, Sandia National Laboratories, Albuquerque, New Mexico, USA*
[4]*Department of Electrical and Computer Engineering, University of California, Santa Barbara, California, USA*
[5]*James C. Wyant College of Optical Sciences, University of Arizona, Tucson, Arizona, USA*

(Received 9 March 2023; accepted 22 February 2024; published 2 April 2024)

Optical nonreciprocity plays a key role in almost every optical system, directing light flow and protecting optical components from backscattered light. Controllable forms of on-chip nonreciprocity are needed for the robust operation of increasingly sophisticated photonic integrated circuits (PICs) in the context of classical and quantum computation, networking, communications, and sensing. However, it has been challenging to achieve wideband, low-loss optical nonreciprocity on-chip. In this paper, we demonstrate strong coupling and Rabi-like energy exchange between photonic bands, possessing a continuum of modes, to unlock nonreciprocity and frequency translation over wide optical bandwidths in silicon. Using a traveling-wave phonon field to drive indirect interband photonic transitions, we demonstrate band hybridization that enables an intriguing form of nonreciprocal dissipation engineering. Using the converted mode to create a nonreciprocal dissipation channel, we demonstrate a frequency-neutral, low-loss (less than 1 dB) isolator with high nonreciprocal contrast (more than 14 dB) and broad operating bandwidth (more than 59 GHz). Additionally, through the implementation of complete interband conversion, we demonstrate a high extinction (more than 55 dB) optical frequency translation operation with near-unity efficiency.

DOI: 10.1103/PhysRevX.14.021002

Subject Areas: Optics, Photonics, Semiconductor Physics

I. INTRODUCTION

The manipulation and control of light using photonic integrated circuits has enabled transformative advances in classical [1,2] and quantum computation [3,4], communications [5,6], and imaging [7–9]. In these on-chip optical systems, optical nonreciprocity is an essential tool that permits us to control the direction of light flow, protecting lasers and other optical components from the destabilizing effects of backscattered light. Traditional methods for achieving integrated nonreciprocity have relied on magneto-optical materials [10,11]; however, their incompatibility with CMOS fabrication has limited their practical use. To address this challenge, time modulated optical systems have been used to demonstrate nonmagnetic isolators through the realization of direction dependent dissipation channels. So far, researchers have employed discrete resonances to effectively dissipate undesired light in the isolation direction by utilizing scattering between resonant modes [12–16], resonant mode hybridization [17–19], or resonator-based spectral filtering [20]. However, since the operational bandwidth of these systems is limited by the spectral bandwidth of cavity resonator, it is challenging to realize wideband integrated optical isolators using this approach.

Alternatively, wideband optical isolation can be realized using a continuum of modes within a band of photonic states to create a nonreciprocal dissipation channel [21]. Prior studies have utilized various mechanisms, such as optomechanical [22–24], electro-optical [25], or nonlinear [26,27] couplings, to facilitate nonreciprocal light scattering between photonic bands. To realize low insertion loss and high contrast isolators, these systems require large coupling rates to produce efficient interband scattering. With the availability of increased coupling rates, it also

*Corresponding author: yishu.zhou@yale.edu
†Corresponding author: peter.rakich@yale.edu

becomes possible to produce hybridization between dynamically coupled photonic bands, corresponding to the strong-coupling regime. If accessible, such band hybridization can enable new nonreciprocal dissipation engineering mechanisms, opening the door to innovative strategies for efficient wideband nonreciprocity.

Here, we demonstrate a novel form of nonreciprocal dissipation engineering achieved through strong coupling between two photonic bands possessing a continuum of modes. Efficient interband scattering is produced using electrically transduced traveling-wave phonons within a multimode optomechanical waveguide. Using an acoustic guided-wave resonance to enhance the phonon field in multipass spiral waveguide geometry, we demonstrate enhanced scattering efficiencies necessary to produce complete interband conversion within the strong coupling regime. This form of strong coupling between optical bands distinguishes itself from the previously reported phonon-photon strong coupling [28–30]. In the presence of a strong phonon drive, the system exhibits Rabi-like interband energy exchange and controllable band hybridization. Using this system to implement complete interband conversion, we demonstrate a high extinction (more than 55 dB) optical frequency translation operation with near-unity efficiency. Phase matching of this indirect interband process also creates an intriguing form of nonreciprocal band hybridization, causing mode conversion at distinct resonance frequencies for forward- and backward-propagating waves. We harness this converted mode to realize a direction-dependent dissipation channel to demonstrate a low-loss (less than 1 dB) isolator with high nonreciprocal contrast (greater than 14 dB) and a broad operating bandwidth (greater than 59 GHz), representing an 80-fold bandwidth enhancement relative to prior nonmagnetic isolators with comparable loss [16–19].

II. CONCEPT

We demonstrate interband strong coupling through the use of a traveling-wave phonon field to drive an optomechanical scattering process in a linear multimode waveguide. Mode multiplexers at the input of the multimode system permit selective excitation of distinct spatial modes of the system [Fig. 1(a) inset]. Optomechanical inter-band coupling is produced by an electromechanically driven counterpropagating acoustic mode, which generates energy exchange between the symmetric optical mode $|1\rangle$ and the antisymmetric optical mode $|2\rangle$ along the propagating z direction [Fig. 1(a)].

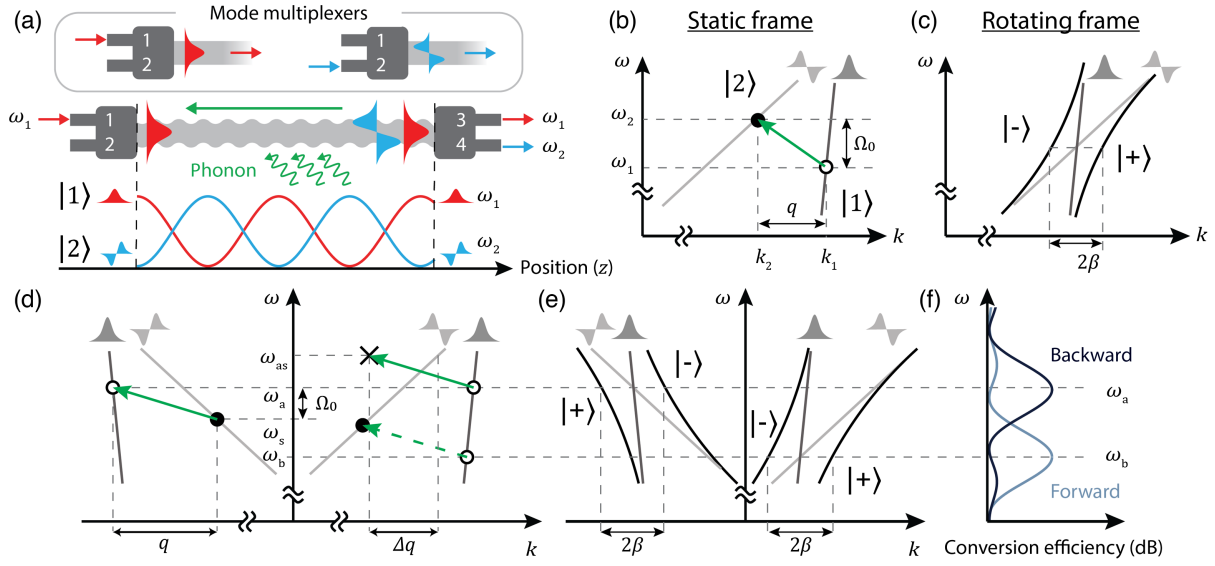

FIG. 1. Strong coupling between two traveling modes. (a) Indirect interband photonic transitions in a multimode, linear waveguide. Two mode multiplexers are fabricated at the ends of the waveguide to selectively couple in and out of each optical mode. A counterpropagating phonon mediates the symmetric (red) to antisymmetric (blue) mode scattering, resulting in a fast energy exchange between the optical modes in the spatial domain. (b),(c) Phase-matching diagram of optomechanical scattering in the static (b) and rotating (c) frames. (b) Phonon with frequency Ω_0 and wave vector $-q$ participating in the optical interband transition (from open to closed circle) when energy conservation $\omega_2 - \omega_1 = \Omega_0$ and momentum conservation $k_1 - k_2 = q$ are satisfied. (c) Rotated optical bands intersecting at the phase-matching point and subsequently split into two new hybrid modes according to the anticrossing principle, which leads to the formation of synthetic band hybridization. As the system deviates from the phase-matching point, the new hybrid mode converges back into the original modes. The wave-vector splitting β at the phase-matching point is determined by the coupling strength. (d),(e) Nonreciprocal photonic band hybridization in the static (d) and rotating (e) frames. In diagram (d), we show that, at ω_a, the Stokes (anti-Stokes) scattering process is (is not) phase matched in the backward (forward) direction, while at frequency ω_b, the phase-matching condition is reversed. In diagram (e), the photonic bands are hybridized at ω_b (ω_a) in the forward (backward) direction, resulting in complete mode conversion in the forward (backward) direction in diagram (f).

The conditions for phonon-mediated band hybridization are described by the phase-matching diagram of Fig. 1(b); scattering occurs when both energy conservation, $\omega_2 = \omega_1 + \Omega_0$, and phase matching, $k_2(\omega_2) = k_1(\omega_1) - q$, are satisfied [31]. Here, q is the longitudinal wave vector of the guided acoustic phonon mode, and $\omega_1(k_1)$ and $\omega_2(k_2)$ are the frequencies (wave vectors) of the guided optical modes. Expressing the ith optical mode $a_i(t,z)|i\rangle$ of the uncoupled system as the product of field amplitude $a_i(t,z) = a_i(0,z)e^{-i\omega_i t}$ and transverse mode profile $|i\rangle$, the equations of motion are

$$\frac{\mathrm{d}}{\mathrm{d}z}\begin{bmatrix} a_1(t,z) \\ a_2(t,z) \end{bmatrix} = \begin{bmatrix} -\frac{1}{2}\alpha_1 & -\frac{i}{v_1}g^* b^*(t,z) \\ -\frac{i}{v_2}gb(t,z) & -\frac{1}{2}\alpha_2 \end{bmatrix} \cdot \begin{bmatrix} a_1(t,z) \\ a_2(t,z) \end{bmatrix}, \tag{1}$$

where α_i and v_i are the spatial decay rate and group velocity of the ith optical mode. The off-diagonal term $gb(t,z)$ represents the intermodal coupling rate, where g is the length-normalized optomechanical coupling rate and $b(t,z) = b(0,z)e^{-i\Omega_0 t}$ is the mean phonon field amplitude. Using a space- and time-dependent unitary matrix to diagonalize the coupling matrix, we see that the modes of the hybridized system are approximated as

$$a_+(t,z)|+\rangle = \frac{1}{\sqrt{2}}[a_1(t,z)|1\rangle - \gamma(t,z)a_2(t,z)|2\rangle], \tag{2}$$

$$a_-(t,z)|-\rangle = \frac{1}{\sqrt{2}}[\gamma(t,z)^{-1}a_1(t,z)|1\rangle + a_2(t,z)|2\rangle], \tag{3}$$

for resonant phase-matching in the strong-coupling limit, where $\gamma(t,z) = (v_1/v_2)^{\frac{1}{2}}[gb(t,z)/|gb(0,z)|]$. (See Sec. II in Supplemental Material [32] for details.) We refer to this acoustically driven band hybridization as "synthetic band hybridization" since each of the hybridized modes, $a_\pm$, contains optical frequency components that oscillate simultaneously at frequencies ω_1 and ω_2. The spatial evolution of these supermodes is described by

$$a_\pm(t,z) = a_\pm(t,0)\ \exp\left(-\frac{1}{2}\alpha z \pm i\beta z\right), \tag{4}$$

where $\alpha = (\alpha_1 + \alpha_2)/2$ is the decay rate and $2\beta \cong 2|gb|/\sqrt{v_1 v_2}$ is the hybridization-induced band splitting depicted in Fig. 1(c). As the system deviates from the phase-matching point, the mode splitting is reduced, ultimately resulting in convergence between the new eigenmodes and the old basis of spatial modes.

Coherent energy exchange produced by interband coupling can be used to implement frequency translation operations. For example, injecting light of frequency ω_1 into the symmetric spatial mode $|1\rangle$ projects the system into a linear combination of supermodes, a_+ and a_-. Interference between these supermodes results in the coherent exchange of light between bands $|1\rangle$ and $|2\rangle$ with a spatial period β of Rabi oscillation [see Fig. 1(a)]. Hence, complete energy transfer from mode $|1\rangle$ to $|2\rangle$ is produced when the phonon drive strength is tuned to meet the condition $L = \pi/\beta$, where L is the device length. Since light in mode $|2\rangle$ oscillates at optical frequency ω_2, this energy conversion also translates the frequency spectrum of the optical field from ω_1 to $\omega_2 = \omega_1 + \Omega$. In Sec. IV, we will use this Rabi-like energy exchange to demonstrate frequency translation through complete energy transfer produced by this interband conversion.

This indirect interband coupling can also be used to implement new forms of nonreciprocal dissipation engineering as the basis for wideband optical isolators. The phase-matching conditions associated with this externally driven traveling-wave phonon field produce a direction dependence on interband coupling. As seen in Fig. 1(d), the conditions for phase-matched interband coupling are satisfied at frequency ω_b for forward-propagating $(+k)$ optical waves, while phase-matched coupling occurs at distinct frequency ω_a for backward-propagating $(-k)$ optical waves. Hence, photonic bands $|1\rangle$ and $|2\rangle$ hybridize at distinct frequencies in the forward and backward directions [Fig. 1(e)], resulting in a maximum of interband conversion at distinct frequencies in the forward and backward directions [Fig. 1(f)]. This complete intermodal energy transfer can be utilized to create a direction-dependent dissipation channel across a wide optical bandwidth. Consequently, the transmitted light is not scattered by the acoustic field and does not inherit any frequency shift, unwanted noise, or distortion from the elastic field. We engineer this nonreciprocal dissipation channel to demonstrate high-performance, wideband optical isolation in Sec. IV.

III. EXPERIMENTAL RESULTS

The physical system under study is an optomechanical device fabricated on an AlN-on-SOI platform using a CMOS foundry process (see Appendix A). This device [Fig. 2(a)] consists of a triple-pass silicon optomechanical waveguide that produces efficient optomechanical scattering when phonons, emitted by a piezoelectric interdigitated transducer (IDT), interact with the waveguide. The IDT consists of 200-nm-thick Al electrodes atop a 480-nm-thick polycrystalline AlN on silicon (150-nm-thick) layer; under a microwave drive at frequency $\Omega_0/(2\pi) \sim 3.1$ GHz, the IDT resonantly excites a traveling-wave phonon mode guided within a silicon optomechanical waveguide. The oxide undercladding is removed from the IDT and the optomechanical waveguide to enhance the phonon confinement and reduce mechanical dissipation. Phonons are confined within the optomechanical waveguide by a phononic crystal on one side and the slots on the opposite side, resulting in a high acoustic quality factor of approximately

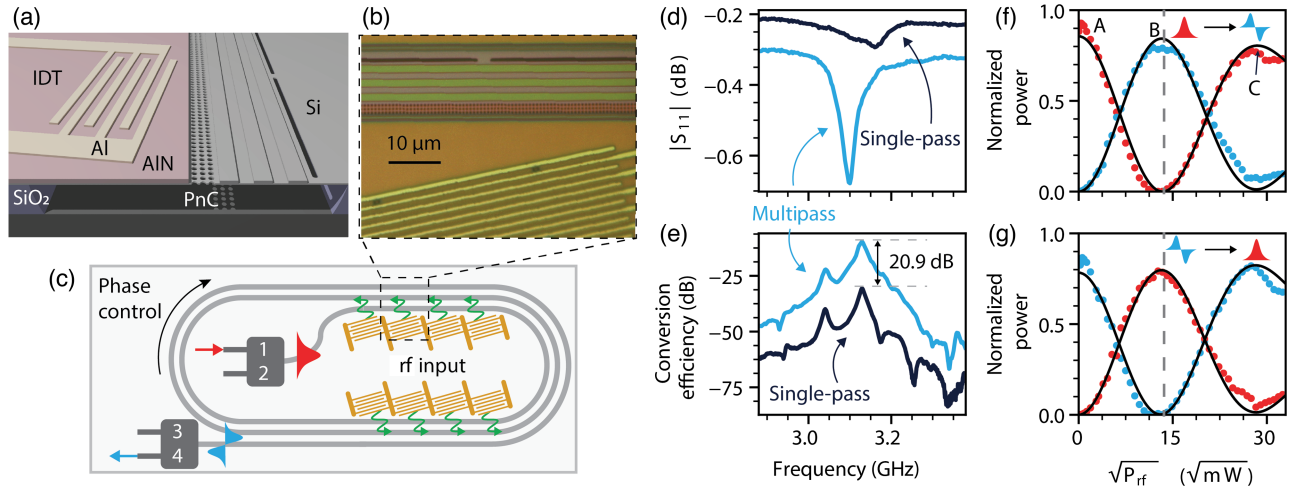

FIG. 2. Device characterization. (a) A 3D rendering of an active unit of the device. An electromechanical transducer launches acoustic waves towards a silicon optomechanical waveguide. The tri-ridge optomechanical waveguide confines an acoustic wave. Each ridge waveguide supports a symmetric and an antisymmetric optical mode. (b) Optical micrograph of the actual device. (c) Spiral-shaped multipass device that connects eight active units, resulting in 24 electro-optomechanical interaction segments (8 units × 3 passes). This result reduces the phonon energy threshold for strong coupling by a factor of 24^2. (d) rf power reflection (S_{11}, measured with a VNA) of a spiral-shaped multipass device (blue) and a single-pass reference device that contains only one IDT unit (black). (e) Optical conversion efficiency of the multipass and single-pass devices, measured using a heterodyne setup. (d),(e) Multipass device featuring more efficient transduction in panel (d) and a 20.9-dB conversion efficiency improvement in panel (e). (f),(g) Rabi-like energy exchanges between the symmetric mode (red) and the antisymmetric mode (blue) for symmetric (antisymmetric) input in panel (f) [(g)]. As P_{rf} increases, the optical power is converted from one mode into the other mode (dashed line) and converted back (point C). The different peak amplitudes at points A, B, and C are determined by the spatial decay rates of the optical modes. From the data at $\sqrt{P_{\mathrm{rf}}} = 0$, we retrieve the linear propagation loss for the symmetric (f) and antisymmetric (g) modes.

$Q \sim 200$. Elastic waves are generated by the IDT tunnel into the acoustic waveguide through the phononic crystal region, yielding resonant enhancement of the elastic wave amplitude as a traveling guided wave is excited. This traveling elastic wave produces phase-matched interband coupling between the optical modes supported by each of the three ridge waveguides patterned in the middle of the optomechanical waveguide. The guided acoustic mode extends over all three optical waveguides, providing a consistent optomechanical coupling rate g between them (Sec. I in Supplemental Material [32]). Figure 2(b) shows a micrograph of the fabricated device.

As discussed in Sec. II, a Rabi-like energy exchange between optical waves propagating in band $|1\rangle$ and band $|2\rangle$ will occur if we can increase βL to meet the conditions for strong coupling. Enhancement of βL can be achieved by either increasing L or by boosting the phonon amplitude $|\bar{b}|$ to increase β, the spatial coupling rate. To leverage this insight, our design integrates eight optomechanical "unit cells" into a multipass spiral waveguide [Fig. 2(c)]. Each unit cell contains an IDT and a short optomechanical waveguide segment of length $L \approx 150$ μm. This design produces a total optomechanical interaction length of $L_{\mathrm{a}} = NL$, where $N = 24$ is the number of optomechanical interaction segments (8 units × 3 passes), which reduces the phonon power required for unity conversion by a factor of N^2.

We first quantify the interband optical mode conversion in the multipass spiral device of Fig. 2(c) in the weak-coupling limit ($\beta L_a \ll 1$). Optical heterodyne spectroscopy is used to identify the spectral components that are frequency shifted through the interband scattering process (see Appendix A). The conversion efficiency of interband scattering from symmetric to antisymmetric optical modes is displayed as a function of rf drive frequency, with $P_{\mathrm{rf}} = 8.92$ dBm, in Fig. 2(e) (blue). Peak mode conversion is observed at $\Omega_0/(2\pi) = 3.13$ GHz, the resonant frequency of the acoustic waveguide mode. We observe a 20.9-dB enhancement in optical conversion efficiency at the resonant frequency in the multipass device [Fig. 2(e), blue] when compared to a reference device that only has a single optomechanical unit cell [$N = 1$; Fig. 2(e), black]. This enhancement matches well to a theoretical prediction of 23.52 dB (Sec. II in Supplemental Material [32]), which accounts for the increase in the number of passes and the transduction efficiency improvement of the IDTs [Fig. 2(d)].

Next, we increase the drive strength to explore the dynamics of the system in the strong-coupling regime. In the strong-coupling limit, injecting light into the symmetric spatial mode $|1\rangle$ will project the system into a linear combination of hybridized bands, a_+ and a_-, whose interference will produce coherent optical exchange between bands $|1\rangle$ and $|2\rangle$. Interference of the two

hybridized modes produces Rabi-like optical exchange, with optical powers $P_1^{\text{out}} \approx P_1^{\text{in}} e^{-\alpha L} \cos^2(\beta L)$ and $P_2^{\text{out}} \approx P_1^{\text{in}} e^{-\alpha L} \sin^2(\beta L)$ in mode $|1\rangle$ and mode $|2\rangle$, respectively. Since β is proportional to the phonon field, the power exchange can be varied by changing the phonon drive strength.

Figure 2(f) shows the normalized optical power in the symmetric (red) and antisymmetric (blue) modes measured at the output of the device as a function of applied rf power, which controls the phonon field amplitude. (Note that these data have been processed to compensate for the thermal shifts in the device response for increasing microwave drive powers. For further details, see Appendix A.) At low rf power (point A), light in the symmetric mode passes through the system unaltered, whereas at intermediate drive power (point B), all power initially in the symmetric mode is swapped into the antisymmetric mode. At strong rf power (point C), the power is converted back into the symmetric mode at the exit of the device. The experimental data show good agreement with a more detailed model that is derived using a transfer matrix method (black lines) (Sec. II in Supplemental Material [32]). Note that the symmetric mode features lower propagation loss ($\alpha_1 \approx 7.0\ \text{m}^{-1}$) than the antisymmetric mode ($\alpha_2 \approx 20.0\ \text{m}^{-1}$), giving rise to different oscillation amplitudes at points A, B, and C. When light is injected into the antisymmetric mode at the device input, we observe a complementary behavior, as seen in Fig. 2(g). Thus, enhancement of the interband coupling in this multipass device configuration enables Rabi-like energy exchange that is characteristic of interband strong coupling. Next, we use this interband strong coupling to demonstrate a variety of photonic functionalities.

IV. OPTICAL FREQUENCY TRANSLATION

Next, we use Rabi-like energy exchange to implement a frequency translation operation. This is accomplished by using a mode multiplexer to selectively excite the antisymmetric mode in band $|2\rangle$ while tuning the microwave drive amplitude to meet the condition $\beta L_a = \pi/2$ necessary for complete interband energy transfer [point B of Fig. 2(f)]. Interband conversion from mode $|2\rangle$ to mode $|1\rangle$ produces complete conversion of the incident optical wave from frequency ω_{p} to frequency $\omega_{\text{p}} - \Omega_0$ at the system output using microwave frequency $\Omega_0/2\pi = 3.13$ GHz and power 22.16 dBm.

Heterodyne spectral analysis of the light exiting mode $|2\rangle$ through the mode multiplexer reveals three tones, including a dominant frequency-shifted Stokes sideband at frequency $\omega_{\text{s}} = \omega_{\text{p}} - \Omega_0$ (red), a residual optical carrier at frequency ω_{p} (blue), and a spurious anti-Stokes sideband at frequency $\omega_{\text{as}} = \omega_{\text{p}} + \Omega_0$ (purple); the conversion efficiency for each of these frequencies is plotted versus the incident optical wavelength in Fig. 3(a). These data reveal a high peak conversion efficiency of −2 dB (63%) and a

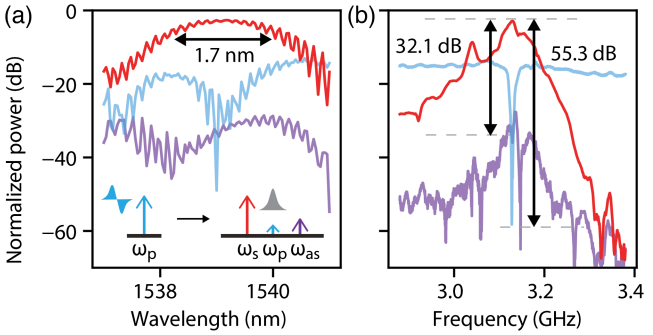

FIG. 3. Optical frequency translation with high efficiency and high extinction. (a) Measuring the output of the symmetric mode of the frequency shifter as a function of optical wavelength and for fixed rf drive frequency $\Omega_0/(2\pi) = 3.13$ GHz. Incident light in the antisymmetric mode at frequency ω_{p} is converted into the symmetric mode with Stokes frequency $\omega_s = \omega_p - \Omega_0$ (red) and anti-Stokes frequency $\omega_{\text{as}} = \omega_p + \Omega_0$ (purple). The symmetric mode also contains a residue at the carrier frequency (blue). Inset: overview of the dominant frequency tones and modes in this experiment. (b) The rf sweep at fixed input wavelength ($\lambda_{\text{p}} = 1539.2$ nm). Colors are similar to panel (a). We achieve an insertion loss of 2 dB, a carrier-suppression ratio of 55.3 dB, and a single-sideband selectivity of 32.1 dB.

3-dB optical bandwidth of interband conversion covering 1.7 nm. Residual light at ω_{p} is consistent with the modal crosstalk at the abrupt waveguide bends (i.e., not due to interband conversion), and a spurious sideband at ω_{as} is likely attributed to the acoustic inhomogeneities (Sec. II in Supplemental Material [32]). At the peak conversion wavelength ($\lambda_{\text{p}} = 1539.2$ nm), interband conversion reaches a maximum value of −2 dB, limited by 1 dB of optical propagation loss (Table I in Appendix B), about 0.2 dB of mode multiplexer loss (Sec. I in Supplemental Material [32]), and about 0.8 dB of loss due to evanescent coupling between adjacent waveguides (Sec. II in Supplemental Material [32]). In future designs, the evanescent coupling loss could be mitigated [33–35].

To investigate the potential for high-spectral-purity frequency-translation operations, we examine the relative magnitude of tones at ω_{s}, ω_{p}, and ω_{as} as a function of the microwave drive frequency. Fixing the incident wavelength for maximum conversion ($\lambda_{\text{p}} = 1539.2$ nm) and sweeping the microwave drive frequency, we observe a maximum carrier suppression of 55.3 dB and sideband suppression of 32.1 dB with optimal rf drive [see Fig. 3(b)], demonstrating the potential utility of such chip-integrated photonic elements for future quantum systems and atomic systems.

V. WIDEBAND NONRECIPROCITY

Next, we use the direction dependence of indirect interband coupling to create new forms of nonreciprocal dissipation engineering necessary for wideband optical isolation. Our system employs this method to selectively

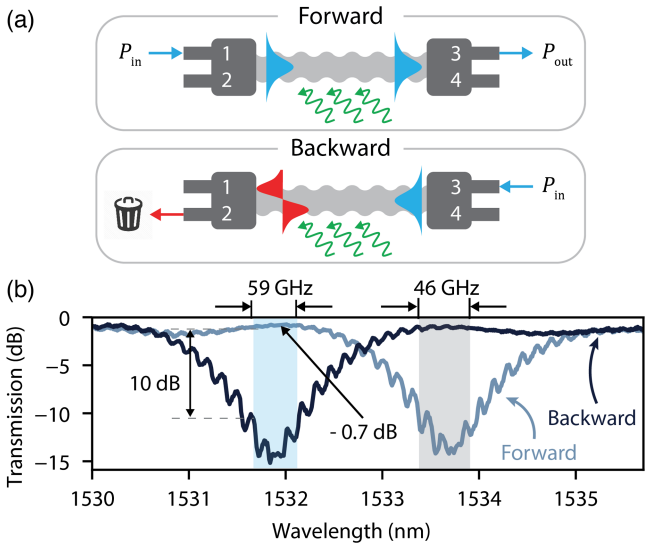

FIG. 4. Wideband, low-loss nonreciprocity. (a) Optomechanical scattering process, which is not phase matched in the forward direction, such that the pump light in the symmetric mode (blue) travels through the device unaltered. The optomechanical scattering is phase matched in the backward direction, such that the pump light is fully converted into the antisymmetric mode (red) and is filtered out by the mode multiplexers. (b) Optical transmission measurement using an optical power meter, showing isolation with 0.7-dB insertion loss and 59-GHz 10-dB isolation bandwidth. The blue (gray) window corresponds to the 10-dB isolation window at ω_a (ω_b). The practical optical power isolation is measured to be 14.4 dB while the frequency-resolved isolation is more than 40 dB according to the heterodyne detection in Sec. II of Supplemental Material [32].

eliminate the scattered antisymmetric mode, creating a direction-dependent loss channel. Specifically, we utilize mode multiplexers to analyze system behaviors, as illustrated in Fig. 4(a), where the interaction between ports 1 and 3 resembles that of an optical isolator. However, mode multiplexers are not necessary; a tapered waveguide can readily be used to produce the same mode filtering operation required for optical isolation.

Nonreciprocity of this system stems from the fact that band hybridization occurs at distinct frequencies for forward- and backward-traveling optical waves (see Sec. II). As seen in Fig. 4(a), an optical wave of frequency ω_a entering port 1 excites a forward-propagating $(+k)$ optical wave in band $|1\rangle$. Since this wave is not phase matched, it propagates unimpeded through the optomechanical waveguide, exiting port 3. No noise is added to the optical field since the acousto-optic scattering process does not occur. However, an optical wave entering port 3 at the same frequency excites a backward-propagating $(-k)$ wave in band $|1\rangle$ to produce phase-matched scattering from $|1\rangle$ to $|2\rangle$ [see Figs. 1(d) and 1(e)]. When the condition $\beta_a L = \pi/2$ is satisfied, complete energy transfer from $|1\rangle$ to $|2\rangle$ occurs, resulting in dissipation of the incident wave through the mode multiplexer. Notice that interband strong coupling is required to implement this form of nonreciprocal dissipation engineering, distinguishing this mechanism from Refs. [20,24,25,31,36,37]. This system produces frequency-neutral, nonreciprocal response as the basis for a practical, wideband optical isolator.

We implement this scheme for frequency-neutral optical isolation by measuring the optical response between port 1 and port 3 while using a microwave drive that produces complete interband mode conversion. A device with minimal intermodal crosstalk is selected for this demonstration, and its parameters are detailed in Table I in Appendix B. Under these conditions, we observe an optical transmission loss of −0.7 dB in the forward direction (port 1 to port 3) at $\lambda = 1532.01$-nm wavelengths (corresponding to ω_a), as seen in Fig. 4(b). By comparison, light injected in the backward direction (port 3 to port 1) at these same wavelengths is rejected, leading to a maximum isolation of 14.4 dB. Through these measurements, an optical power meter was used to detect the total optical power transmission in the forward and backward directions. Wavelength-dependent power transmission measurements in the forward and backward directions reveal high isolation contrast (10 dB) over an appreciable (59 GHz) bandwidth indicated by the shaded blue region in Fig. 4(b).

It is worth noting that this system also functions as an isolator in the opposite direction over a second band of wavelengths centered around a different optical frequency ω_b [indicated by the gray window in Fig. 4(b)], where the photonic bands hybridize in the forward direction [Fig. 1(e)]. At this frequency, backward light is fully transmitted, and forward light is dissipated.

The isolation contrast of 14.4 dB, which was obtained by measuring the total optical power transmission, can be greatly improved with minor design modifications. The isolation contrast of this system is limited by intermodal crosstalk generated by waveguide bend transitions and spurious evanescent coupling of the adjacent waveguides. Using heterodyne measurement to analyze the spectral content of light transmitted in the backward direction, we see that this system exhibits a transmission contrast greater than 40 dB if we apply a more formal definition of nonreciprocity (i.e., ignoring the presence of these unwanted tones). (See Sec. II of Supplemental Material [32].) Hence, significantly higher (30–40 dB) nonreciprocal transition should be accessible by adding extra optical filters that would remove spurious tones resulting from crosstalk, mitigating crosstalk by minimizing evanescent mode coupling, or cascading a few optomechanical isolators.

VI. CONCLUSION AND DISCUSSION

We have shown that strong coupling and Rabi-like energy exchange between photonic bands, possessing a continuum of modes, can be used to demonstrate frequency translation and new strategies for wideband nonreciprocity.

Using a traveling-wave phonon field to drive indirect interband photonic transitions, we observed an intriguing form of nonreciprocal band hybridization. Using this system to implement complete interband conversion, we demonstrated a high extinction (greater than 55 dB) optical frequency translation operation with near-unity efficiency.

Utilizing complete interband conversion in conjunction with the nonreciprocal nature of the band hybridization, we created a direction-dependent dissipation channel and engineered it to demonstrate a nonmagnetic isolator. Through this approach, we demonstrated a frequency-neutral, low-loss (0.7-dB) isolator with high nonreciprocal contrast (14.4 dB) and broad operating bandwidth (greater than 59 GHz). Relative to prior demonstrations of nonreciprocity with resonator-based systems having discrete modes [12–19], greatly extended isolation bandwidths produced here are enabled by interband transitions between a continuum of optical modes.

Building on these concepts, systems with tailorable driven interband transitions could offer a way to access intriguing new dynamics by leveraging fruitful analogies between optical, atomic, and condensed matter physics. For example, by simultaneously driving two or more interband transitions within a system that possesses a larger number of optical modes, it is possible to create more complex synthetic band hybridization. By engineering the spatial decay rates of multiple photon modes, it may be possible to extend non-Hermitian physics and exceptional points [38] to continuous systems. Moreover, by controlling the phase of the coupling strength of each interband transition, one could explore Aharonov-Bohm interference and topological complex-energy braiding in the spatial-temporal domain [39–41].

ACKNOWLEDGMENTS

We thank Yanni Dahmani for the discussion on the electromechanical transducer designs and Taekwan Yoon for proofreading the manuscript. This research was developed with funding from the Defense Advanced Research Projects Agency (DARPALUMOS) (HR0011048577). This material is based upon work supported by the Laboratory Directed Research and Development program at Sandia National Laboratories. Sandia National Laboratories is a multiprogram laboratory managed and operated by National Technology and Engineering Solutions of Sandia, LLC, a wholly owned subsidiary of Honeywell International, Inc., for the U.S. Department of Energy's National Nuclear Security Administration under Contract No. DE-NA-0003525. This paper describes objective technical results and analyses. The views, opinions, and/or findings expressed are those of the authors and should not be interpreted as representing the official views or policies of the U.S. Department of Energy, U.S. Department of Defense, or the U.S. Government. Part of the research was carried out at the Jet Propulsion Laboratory, California Institute of Technology, under a contract with the National Aeronautics and Space Administration. This research was developed with funding from the Defense Advanced Research Projects Agency (DARPA LUMOS) under Grant No. HR0011048577 and the National Science Foundation (NSF) under Grant No. 2137740.

The views, opinions and/or findings expressed are those of the author and should not be interpreted as representing the official views or policies of the Department of Defense, National Science Foundation, or the U.S. Government.

APPENDIX A: EXPERIMENTAL DETAILS

1. Device fabrication

The silicon photonic acousto-optic frequency shifter and isolator devices are fabricated on single-crystal silicon-on-insulator (SOI) wafers using Sandia's Microsystems and Engineering, Sciences and Applications (MESA) CMOS production and research facilities. Features in the silicon, oxide, aluminum nitride, and aluminum metal are patterned and defined with deep-UV photolithography and plasma etching. After processing the optical and acoustic waveguide structures in the silicon device layer, we deposit 8000 Å of plasma-enhanced chemical-vapor-deposited (PECVD) oxide and employ chemical mechanical polishing (CMP) to thin the oxide to the desired thickness (about 3000 Å), which serves as a mask and etch stop for the subsequent AlN and Al layers, respectively. The 4800-Å AlN piezoelectric film is deposited using rf sputtering such that the c axis of the crystal grains is oriented normal to the wafer plane (fiber texture). The electrodes are defined and patterned in a 2000-Å-thick aluminum film. Suspended structures are created through a vapor-hydrogen-fluoride (VHF) release process at the die level, which removes the top oxide etch mask and undercuts a targeted distance of the device layer through defined openings to the 3-μm buried oxide.

2. IDT characterization

Figure 5(a) shows a micrograph of the fabricated device. The eight IDT units of our multipass device are wired to five electrical contact pads and connected to a dual-channel rf probe in a GSGSG (ground-signal) configuration. Each rf signal pin drives four IDTs, and the relative phase between each pin is controlled by an external microwave phase shifter.

We perform the S_{11} measurements on the IDTs using a vector network analyzer (VNA, Keysight p5004A) that connects to a rf probe (FormFactor I40, pitch 100 micron) in the GSG or GSGSG configuration. As displayed in the main text in Figs. 2(d) and 2(e), both the four-unit and one-unit IDT exhibit a resonance (dip in reflection) at rf $\Omega_0/(2\pi) \approx 3.1$ GHz. Interestingly, the four-unit subsystem that is used in the multipass device (blue)

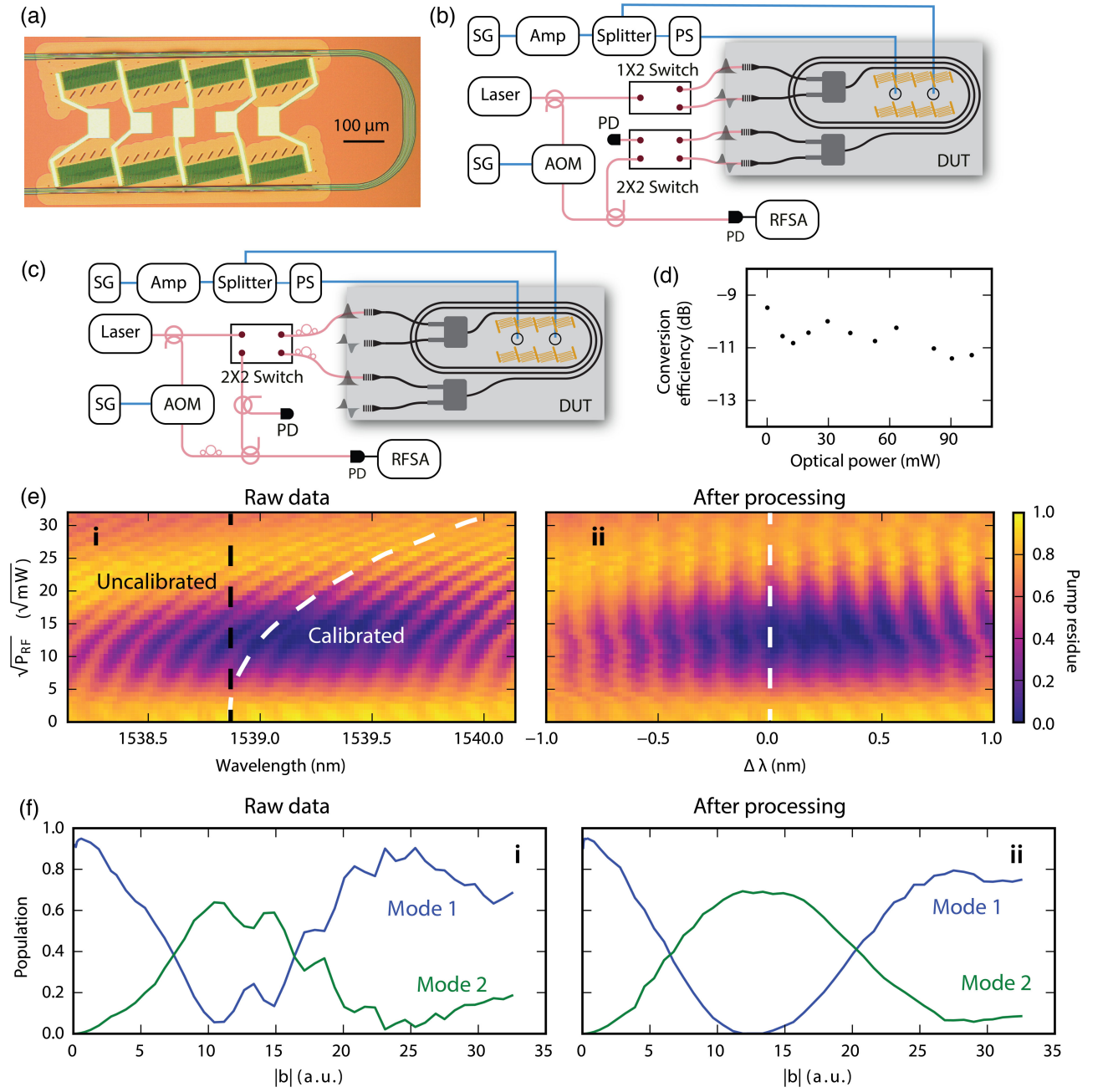

FIG. 5. Further experimental details. (a) Optical micrographs of the fabricated device. (b) Experimental setup to study the optical mode conversion. A rf signal drives two (50/50) IDT channels, where an external phase shifter is used for phase control. Light is injected into the symmetric (antisymmetric) mode to characterize optical mode conversion. An optical 2×2 switch is used to perform either an optical power measurement or a frequency-resolved measurement using heterodyne detection. SG, signal generator; Amp, rf amplifier; Splitter, 50/50 power splitter; PS, rf phase shifter; AOM, acousto-optic modulator; PD, photodiode; and RFSA, rf spectral analyzer. (c) Experimental setup to characterize the isolator. A 2×2 switch allows rapid measurements of the device in forward or backward operation; using a directional coupler, we perform a frequency-resolved measurement (heterodyne detection) and optical power measurement (optical power meter). (d) Device robustness to optical power. When increasing the on-chip optical power to 100 mW, our device only features about 2-dB conversion efficiency deterioration, which we attribute to nonlinear loss mechanisms in silicon. (e) Raw (i) and processed (ii) data of Rabi-like energy exchange measurement. Here, we measure the symmetric-to-symmetric mode conversion efficiency as a function of optical wavelength and rf drive power. We expect a periodic modulation of the conversion efficiency when sweeping the wavelength, given the presence of evanescent coupling between adjacent waveguides. Thus, the skewed modulation in (i) is used to track and correct thermal drift at high rf power. A line cut at $\Delta\lambda = 0$ in (ii) corresponds to the red data points in Fig. 2(f). Panel (fi) displays the line cut of the raw data, as indicated by the black dashed line in (ei), taken at 1538.8 nm, which corresponds to the phase-matched wavelength at low microwave input. Panel (fii) presents the processed line cut of the Rabi oscillations, as denoted by the white dashed line in (ei) or the white solid line in (eii).

exhibits a more significant dip in the S_{11} spectrum when compared to the single-IDT reference device (black). This disparity follows from the larger transducer area in the four-unit IDT system when compared to the surface area for a single IDT. As a result, the four-unit transducer is better impedance matched to our 50-Ohm microwave input [42,43]. We note that better electro-acoustic impedance matching can be achieved by using larger transducer areas than the ones employed here, where a one-unit IDT measures an area A of $A \approx 150\ \mu\text{m} \times 43\ \mu\text{m}$—the need to suspend our devices limits the area that we can use in practice.

3. Optical measurement

a. Mode conversion characterization

To investigate the optical mode conversion process in our device (measurements shown in the main text, Figs. 2 and 3), we use the spectroscopy setup illustrated in Fig. 5(b). We drive the phonons in our system—via the IDTs—with a rf signal that is obtained from a signal generator (SG, Agilent E8257D). Before entering the device under test (DUT), the output from the signal generator is sent to a tunable amplifier (Mini-Circuits ZHL-5W-63-S+) and divided equally (Mini-Circuits ZX10-2-183-S+) between two channels. The phase difference between the two rf channels is fine-tuned by a phase shifter (PS, Fairview Microwave SMP0820) to compensate for phase imperfections. The amplified and divided rf signals are sent to the IDTs using a FormFactor I40 five-point probe (100-micron pitch) in a GSGSG configuration that drives the set of 2×4 IDTs in our multipass design. For the reference device with a single-unit IDT, we directly connect the output from the amplifier to a similar three-point probe model (GSG) that drives the single-unit IDT. To study the dynamics of optical mode conversion, light from a tunable telecom wavelength laser (Santec TSL-710, typical power of 10 mW) is split into two arms. One arm is sent into an acousto-optic oscillator (AOM, Brimrose AMF-55-4-1545) driven 55 MHz and used as a local oscillator (LO) for heterodyne detection. The other arm is sent to a 1×2 optical switch (Fiberstore optomechanical optical switch) to alternatively couple into the symmetric or antisymmetric mode of the DUT. This input light provides an on-chip power of approximately 1 mW. We monitor the device output with two techniques using a 2×2 optical switch (Fiberstore optomechanical optical switch). A heterodyne experiment provides access to a frequency-resolved measurement. The output from the device is combined with the LO, then sent to a fast photodiode (Nortel PP-10G) and analyzed using a rf spectrum analyzer (Agilent N9030A PXA Signal Analyzer). Additionally, an optical power meter (PD: Santec MPM-210) gives quick access to the total optical power present in either output port.

b. Isolator characterization

The experimental setup shown in Fig. 5(c) is used for characterizing the isolator, of which the results are shown in Fig. 4 (main text). This setup shares the same group of experimental instruments as Fig. 5(b). In this experiment, a 2×2 optical switch is used to alternatively measure the forward and backward transmission of DUT. The output from DUT is routed back into the optical switch and subsequently divided into two paths for frequency-resolved optical power measurement and total output power measurement.

c. Device robustness to optical power

In our experiment, we typically limit the on-chip optical power to about 1 mW to avoid nonlinear optical absorption. Nevertheless, our device is robust for a range of optical input powers, mainly due to the lack of (strong) optical resonances. In Fig. 5(b), we present the conversion efficiency measurement of a multipass device (device 1) for optical input powers between 0 and 100 mW. The optical wavelength (about 1549.2 nm) and the rf input power (8.92 dBm) are both fixed during these measurements. We observe only a small decrease (about 2 dB) in optical conversion efficiency when injecting a large amount of optical power. We attribute this small decrease in performance to nonlinear absorption (TPA and FCA) of silicon [31].

d. Data analysis for Rabi-like power exchange

We obtain the Rabi-like energy exchange data [Fig. 2(f)] while simultaneously sweeping the optical wavelength and rf drive power. We present the raw data for this measurement in Fig. 5(bi), where the symmetric-mode–to–symmetric-mode scattering efficiency is plotted as a function of the pump optical wavelength and the square root of rf power. The dark stripes in the plot are consistent with the fringes that we observe in Figs. 3(a) and 4(b), which are all caused by the evanescent coupling between the adjacent waveguides. This coupling results in "artificial" ring resonances that should exhibit vertical stripes in the 2D plot, as we explain in Sec. II. I of Supplemental Material [32]. However, the use of large rf power leads to thermal drift in wavelength; thus, the vertical strips become skewed. By tracking these "skewed fringes," we correct for the thermal drift in Fig. 5(bii). In particular, we utilize a peak detection algorithm to detect the fringes caused by the "artificial rings" and calculate their wavelength detuning $\Delta\lambda$ from the center wavelength, i.e., the wavelength that corresponds to the most efficient mode conversion. By remapping the data points into the new x axis—the relative wavelength vs the absolute wavelength—we can obtain the processed data with nearly vertical stripes that match well with our theory in Fig. S8(d) of Supplemental Material [32]. The red points in Fig. 2(f) are actually the

TABLE I. Device parameters. Notice that the source of the parameters is indicated in the footnote. In addition, the dots indicate that it is either not measured or not discussed in this work.

Device parameters	Device 1	Device 2	Device 3	Single-pass reference
IDT pitch (nm)[a]	1675	1675	1750	1675
IDT angle (deg)[a]	12.5772	12.9871	13.5795	12.5772
Total device length L_{tot} (mm)[a]	⋯	9.95	9.95	⋯
Active region length L (μm)[a,f]	138.46	149.07	149.07	138.46
Each segment length d_i (μm)[a,f]	⋯	{149.07, 149.07, 149.07, 804.95, 149.07, 149.07, 149.07, 2310.55, 149.07, 149.07, 149.07, 819.85, 149.07, 149.07, 149.07, 2340.35, 149.07, 149.07, 149.07, 864.66, 149.07, 149.07, 149.07, 149.07}	Same as device 2	⋯
Phononic crystal pitch (nm)[a]	688	688	688	688
Phononic crystal hole radius (nm)[a]	264.88	264.88	264.88	264.88
Acoustic resonance (GHz)[b]	$3.13 \cdot (2\pi)$	$3.13 \cdot (2\pi)$	$3.02 \cdot (2\pi)$	$3.13 \cdot (2\pi)$
rf power for unity conversion (dBm)[b]	⋯	22.16	29.49	⋯
$1 - \lvert S_{11}(\Omega_0)\rvert^2$[b]	16.01%	⋯	⋯	3.70%
Γ (MHz)[b]	$17.74 \cdot (2\pi)$	$22.00 \cdot (2\pi)$	⋯	$13.52 \cdot (2\pi)$
α_1 (m^{-1})[c]	⋯	7.00	⋯	⋯
α_2 (m^{-1})[c]	⋯	20.00	⋯	⋯
f_{scaling}[c]	⋯	1.017	⋯	⋯
κ (m^{-1})[d]	⋯	50	50	⋯
μ (m^{-1})[d]	⋯	285	285	⋯
$n_{\mathrm{eff},1}$[e]	⋯	2.8113	⋯	⋯
$n_{\mathrm{eff},2}$[e]	⋯	2.7042	⋯	⋯
$n_{\mathrm{g},1}$[e]	⋯	3.7869	⋯	⋯
$n_{\mathrm{g},2}$[e]	⋯	3.8959	⋯	⋯
$\lvert g\rvert$ ($\mathrm{Hz} \cdot \sqrt{\mathrm{m}}$)[e]	715.46	715.46	⋯	715.46

[a]Device designs.
[b]Experimental measurements.
[c]Figures 2(f) and 2(g) fitting. The spatial decay rates obtained here are consistent with our previous measurements [31].
[d]The coupling rates are estimated by comparing the experimental data to the calculations in Sec. II. I of Supplemental Material [32].
[e]COMSOL simulations. The parameters listed here are simulated using the 1.5-μm-wide straight waveguide.
[f]The lengths listed here ignore the widths of IDT buses. The actual design including the bus widths deviates from the perfect phase control condition.

line cuts at $\Delta\lambda = 0$ from the 2D plot in Fig. 5(eii). We also present the line cuts of the raw data and the processed data in Fig. 5. Here, we observe that the thermal shift in the raw data could lead to an erroneous underestimation of the Rabi cycle, resulting in an overestimation of our device's scattering efficiency. This observation underscores the necessity of our signal processing to calibrate the thermal shifts, thereby more accurately reflecting the device's true scattering performance.

The black lines in Figs. 2(f) and 2(g) are obtained from a fit procedure using Eq. (S23) in Supplemental Material [32], with the fitting parameters listed in Table I. For the fit. we assume that the spatial decay rate for each mode is constant across the device. The effective indices for the two optical modes are obtained from a 2D COMSOL simulation. In reality, however, our structure contains waveguide bends and waveguide tapering to connect the 1.5-μm and 1.495-μm-wide waveguide sections, leading to a varying mode index along the device that is not captured by our simple COMSOL model. To account for the discrepancy between simulation and experiment, we introduce an extra fitting parameter f_{scaling} to capture the deviation between the simulated and realized (effective) mode indexes. Mathematically, this reads $n_{\mathrm{eff},i}^{\mathrm{average}} \equiv f_{\mathrm{scaling}} n_{\mathrm{eff},i}^{1.5\ \mu\mathrm{m}}$, where $n_{\mathrm{eff},i}^{1.5\ \mu\mathrm{m}}$ is the mode index for mode i that is obtained from COMSOL. From our fit, we obtain $f_{\mathrm{scaling}} = 1.017$, indicating that our experimental system experiences an average 1.7% deviation of effective mode indices when compared to the values obtained from simulation.

APPENDIX B: DEVICES—EXPERIMENTAL PARAMETERS

In this paper, we present measurements from three different devices: device 1 for the single-to-multipass comparison measurements in Figs. 2(d) and 2(e); device 2 for

Rabi measurements and the frequency shifter demonstration in Figs. 2(f), 2(g), 3(a), and 3(b); and device 3 for the isolation measurements in Fig. 4(b). All the multipass devices have 24 segments (3 passes × 8 IDT units), each of which consists of an active region of length L. The total (passive) length of the ith segment is d_i (l_i), such that $d_i = l_i + L$. The total device length is then calculated as $L_{\text{tot}} = \sum_{i=1}^{24} d_i$. We present the device parameters in Table I.

[1] Y. Shen, N. C. Harris, S. Skirlo, M. Prabhu, T. Baehr-Jones, M. Hochberg, X. Sun, S. Zhao, H. Larochelle, D. Englund *et al.*, *Deep learning with coherent nanophotonic circuits*, Nat. Photonics **11**, 441 (2017).

[2] J. Feldmann, N. Youngblood, M. Karpov, H. Gehring, X. Li, M. Stappers, M. Le Gallo, X. Fu, A. Lukashchuk, A. S. Raja *et al.*, *Parallel convolutional processing using an integrated photonic tensor core*, Nature (London) **589**, 52 (2021).

[3] A. Sipahigil, R. E. Evans, D. D. Sukachev, M. J. Burek, J. Borregaard, M. K. Bhaskar, C. T. Nguyen, J. L. Pacheco, H. A. Atikian, C. Meuwly *et al.*, *An integrated diamond nanophotonics platform for quantum-optical networks*, Science **354**, 847 (2016).

[4] G. Moody, V. J. Sorger, D. J. Blumenthal, P. W. Juodawlkis, W. Loh, C. Sorace-Agaskar, A. E. Jones, K. C. Balram, J. C. Matthews, A. Laing *et al.*, *2022 roadmap on integrated quantum photonics*, J. Phys. **4**, 012501 (2022).

[5] G. Roelkens, L. Liu, D. Liang, R. Jones, A. Fang, B. Koch, and J. Bowers, *III-V/silicon photonics for on-chip and intra-chip optical interconnects*, Laser Photonics Rev. **4**, 751 (2010).

[6] A. Rizzo, A. Novick, V. Gopal, B. Y. Kim, X. Ji, S. Daudlin, Y. Okawachi, Q. Cheng, M. Lipson, A. L. Gaeta *et al.*, *Massively scalable Kerr comb-driven silicon photonic link*, Nat. Photonics **17**, 781 (2023).

[7] J. Riemensberger, A. Lukashchuk, M. Karpov, W. Weng, E. Lucas, J. Liu, and T. J. Kippenberg, *Massively parallel coherent laser ranging using a soliton microcomb*, Nature (London) **581**, 164 (2020).

[8] B. Li, Q. Lin, and M. Li, *Frequency–angular resolving LiDAR using chip-scale acousto-optic beam steering*, Nature (London) **620**, 316 (2023).

[9] R. Chen, H. Shu, B. Shen, L. Chang, W. Xie, W. Liao, Z. Tao, J. E. Bowers, and X. Wang, *Breaking the temporal and frequency congestion of LiDAR by parallel chaos*, Nat. Photonics **17**, 306 (2023).

[10] L. Bi, J. Hu, P. Jiang, D. H. Kim, G. F. Dionne, L. C. Kimerling, and C. A. Ross, *On-chip optical isolation in monolithically integrated non-reciprocal optical resonators*, Nat. Photonics **5**, 758 (2011).

[11] Y. Zhang, Q. Du, C. Wang, T. Fakhrul, S. Liu, L. Deng, D. Huang, P. Pintus, J. Bowers, C. A. Ross, J. Hu, and L. Bi, *Monolithic integration of broadband optical isolators for polarization-diverse silicon photonics*, Optica **6**, 473 (2019).

[12] Z. Shen, Y.-L. Zhang, Y. Chen, C.-L. Zou, Y.-F. Xiao, X.-B. Zou, F.-W. Sun, G.-C. Guo, and C.-H. Dong, *Experimental realization of optomechanically induced non-reciprocity*, Nat. Photonics **10**, 657 (2016).

[13] F. Ruesink, M.-A. Miri, A. Alù, and E. Verhagen, *Non-reciprocity and magnetic-free isolation based on optomechanical interactions*, Nat. Commun. **7**, 13662 (2016).

[14] K. Fang, J. Luo, A. Metelmann, M. H. Matheny, F. Marquardt, A. A. Clerk, and O. Painter, *Generalized non-reciprocity in an optomechanical circuit via synthetic magnetism and reservoir engineering*, Nat. Phys. **13**, 465 (2017).

[15] K. Y. Yang, J. Skarda, M. Cotrufo, A. Dutt, G. H. Ahn, M. Sawaby, D. Vercruysse, A. Arbabian, S. Fan, A. Alù, and J. Vučković, *Inverse-designed non-reciprocal pulse router for chip-based LiDAR*, Nat. Photonics **14**, 369 (2020).

[16] J. F. Herrmann, V. Ansari, J. Wang, J. D. Witmer, S. Fan, and A. H. Safavi-Naeini, *Mirror symmetric on-chip frequency circulation of light*, Nat. Photonics **16**, 603 (2022).

[17] D. B. Sohn, O. E. Örsel, and G. Bahl, *Electrically driven optical isolation through phonon-mediated photonic Autler-Townes splitting*, Nat. Photonics **15**, 822 (2021).

[18] H. Tian, J. Liu, A. Siddharth, R. N. Wang, T. Blésin, J. He, T. J. Kippenberg, and S. A. Bhave, *Magnetic-free silicon nitride integrated optical isolator*, Nat. Photonics **15**, 828 (2021).

[19] A. D. White, G. H. Ahn, K. V. Gasse, K. Y. Yang, L. Chang, J. E. Bowers, and J. Vučković, *Integrated passive nonlinear optical isolators*, Nat. Photonics **17**, 143 (2023).

[20] M. Yu, R. Cheng, C. Reimer, L. He, K. Luke, E. Puma, L. Shao, A. Shams-Ansari, X. Ren, H. R. Grant *et al.*, *Integrated electro-optic isolator on thin-film lithium niobate*, Nat. Photonics **17**, 666 (2023).

[21] Z. Yu and S. Fan, *Complete optical isolation created by indirect interband photonic transitions*, Nat. Photonics **3**, 91 (2009).

[22] M. S. Kang, A. Butsch, and P. S. J. Russell, *Reconfigurable light-driven opto-acoustic isolators in photonic crystal fibre*, Nat. Photonics **5**, 549 (2011).

[23] E. A. Kittlaus, N. T. Otterstrom, P. Kharel, S. Gertler, and P. T. Rakich, *Non-reciprocal interband brillouin modulation*, Nat. Photonics **12**, 613 (2018).

[24] E. A. Kittlaus, W. M. Jones, P. T. Rakich, N. T. Otterstrom, R. E. Muller, and M. Rais-Zadeh, *Electrically driven acousto-optics and broadband non-reciprocity in silicon photonics*, Nat. Photonics **15**, 43 (2021).

[25] H. Lira, Z. Yu, S. Fan, and M. Lipson, *Electrically driven nonreciprocity induced by interband photonic transition on a silicon chip*, Phys. Rev. Lett. **109**, 033901 (2012).

[26] S. Signorini, M. Mancinelli, M. Borghi, M. Bernard, M. Ghulinyan, G. Pucker, and L. Pavesi, *Intermodal four-wave mixing in silicon waveguides*, Photon. Res. **6**, 805 (2018).

[27] N. T. Otterstrom, S. Gertler, E. A. Kittlaus, M. Gehl, A. L. Starbuck, C. M. Dallo, A. T. Pomerene, D. C. Trotter, P. T. Rakich, P. S. Davids *et al.*, *Nonreciprocal frequency domain beam splitter*, Phys. Rev. Lett. **127**, 253603 (2021).

[28] S. Gröblacher, K. Hammerer, M. R. Vanner, and M. Aspelmeyer, *Observation of strong coupling between a micromechanical resonator and an optical cavity field*, Nature (London) **460**, 724 (2009).

[29] G. Enzian, M. Szczykulska, J. Silver, L. Del Bino, S. Zhang, I. A. Walmsley, P. Del'Haye, and M. R. Vanner, *Observation*

of brillouin optomechanical strong coupling with an 11 GHz mechanical mode, Optica **6**, 7 (2019).

[30] P. Kharel, Y. Chu, D. Mason, E. A. Kittlaus, N. T. Otterstrom, S. Gertler, and P. T. Rakich, *Multimode strong coupling in cavity optomechanics*, Phys. Rev. Appl. **18**, 024054 (2022).

[31] E. A. Kittlaus, N. T. Otterstrom, and P. T. Rakich, *On-chip inter-modal brillouin scattering*, Nat. Commun. **8**, 15819 (2017).

[32] See Supplemental Material at http://link.aps.org/supplemental/10.1103/PhysRevX.14.021002 for theoretical framework, additional details on device characterization, and a comparison of the device's performance with state-of-the-art metrics.

[33] W. Song, R. Gatdula, S. Abbaslou, M. Lu, A. Stein, W. Y.-C. Lai, J. Provine, R. F. W. Pease, D. N. Christodoulides, and W. Jiang, *High-density waveguide superlattices with low crosstalk*, Nat. Commun. **6**, 7027 (2015).

[34] M. Mrejen, H. Suchowski, T. Hatakeyama, C. Wu, L. Feng, K. O'Brien, Y. Wang, and X. Zhang, *Adiabatic elimination-based coupling control in densely packed subwavelength waveguides*, Nat. Commun. **6**, 7565 (2015).

[35] S. Jahani, S. Kim, J. Atkinson, J. C. Wirth, F. Kalhor, A. A. Noman, W. D. Newman, P. Shekhar, K. Han, V. Van, R. G. DeCorby, L. Chrostowski, M. Qi, and Z. Jacob, *Controlling evanescent waves using silicon photonic all-dielectric metamaterials for dense integration*, Nat. Commun. **9**, 1893 (2018).

[36] Q. Liu, H. Li, and M. Li, *Electromechanical brillouin scattering in integrated optomechanical waveguides*, Optica **6**, 778 (2019).

[37] C. J. Sarabalis, R. V. Laer, R. N. Patel, Y. D. Dahmani, W. Jiang, F. M. Mayor, and A. H. Safavi-Naeini, *Acousto-optic modulation of a wavelength-scale waveguide*, Optica **8**, 477 (2021).

[38] K. Ding, C. Fang, and G. Ma, *Non-Hermitian topology and exceptional-point geometries*, Nat. Rev. Phys. **4**, 745 (2022).

[39] K. Wang, A. Dutt, C. C. Wojcik, and S. Fan, *Topological complex-energy braiding of non-Hermitian bands*, Nature (London) **598**, 59 (2021).

[40] Y. S. S. Patil, J. Höller, P. A. Henry, C. Guria, Y. Zhang, L. Jiang, N. Kralj, N. Read, and J. G. E. Harris, *Measuring the knot of non-Hermitian degeneracies and non-commuting braids*, Nature (London) **607**, 271 (2022).

[41] J. del Pino, J. J. Slim, and E. Verhagen, *Non-Hermitian chiral phononics through optomechanically induced squeezing*, Nature (London) **606**, 82 (2022).

[42] C. Hartmann, D. Bell, and R. Rosenfeld, *Impulse model design of acoustic surface-wave filters*, IEEE Trans. Microwave Theory Tech. **21**, 162 (1973).

[43] Y. D. Dahmani, C. J. Sarabalis, W. Jiang, F. M. Mayor, and A. H. Safavi-Naeini, *Piezoelectric transduction of a wavelength-scale mechanical waveguide*, Phys. Rev. Appl. **13**, 024069 (2020).